Ultrafast laser inscribed waveguide lasers in Tm:CALGO with depressed-index cladding

Victor Llamas, Pavel Loiko, Esrom Kifle, Carolina Romero, Javier Vázquez de Aldana, Zhongben Pan, Josep Maria Serres, Hualei Yuan, Xiaojun Dai, Huaqiang Cai, et al.

Ultrafast laser inscribed waveguide lasers in Tm:CALGO with depressed-index cladding

VICTOR LLAMAS,[1,2] PAVEL LOIKO,[3] ESROM KIFLE,[1] CAROLINA ROMERO,[4] JAVIER R. VÁZQUEZ DE ALDANA,[4] ZHONGBEN PAN,[5,6] JOSEP MARIA SERRES,[1,2] HUALEI YUAN,[5] XIAOJUN DAI,[5] HUAQIANG CAI,[5] YICHENG WANG,[6] YONGGUANG ZHAO,[6,7] VIKTOR ZAKHAROV,[8] ANDREY VENIAMINOV,[8] ROMAIN THOUROUDE,[2] MATHIEU LAROCHE,[2] HERVÉ GILLES,[2] MAGDALENA AGUILÓ,[1] FRANCESC DÍAZ,[1] UWE GRIEBNER,[6] VALENTIN PETROV,[6] PATRICE CAMY,[2] AND XAVIER MATEOS[1,*]

[1]Física i Cristal·lografia de Materials i Nanomaterials (FiCMA-FiCNA)-EMaS, Dept. Química Física i Inòrganica, Universitat Rovira i Virgili (URV), Campus Sescelades, 43007 Tarragona, Spain
[2]Eurecat, Centre Tecnològic de Catalunya, Unitat Advanced Manufacturing Systems (AMS), Campus Sescelades, 43007 Tarragona, Spain
[3]Centre de recherche sur les Ions, les Matériaux et la Photonique (CIMAP), UMR 6252 CEA-CNRS-ENSICAEN, Université de Caen, 6 Boulevard du Maréchal Juin, 14050 Caen Cedex 4, France
[4]Aplicaciones del Láser y Fotónica, University of Salamanca, 37008 Salamanca, Spain
[5]Institute of Chemical Materials, China Academy of Engineering Physics, 621900 Mianyang, China
[6]Max Born Institute for Nonlinear Optics and Short Pulse Spectroscopy, Max-Born-Str. 2a, 12489 Berlin, Germany
[7]Jiangsu Key Laboratory of Advanced Laser Materials and Devices, Jiangsu Normal University, 221116 Xuzhou, China
[8]ITMO University, 49 Kronverkskiy Pr., 197101 St. Petersburg, Russia
**xavier.mateos@urv.cat*

Abstract: Depressed-index buried and surface channel waveguides (type III) are produced in a bulk 3.5 at.% Tm^{3+}:CALGO crystal by femtosecond direct-laser-writing at kHz repetition rate. The waveguides are characterized by confocal microscopy and μ-Raman spectroscopy. Under in-band-pumping at 1679 nm ($^3H_6 \rightarrow {}^3F_4$ transition) by a Raman fiber laser, the buried channel waveguide laser with a circular cladding (diameter: 60 μm) generated a continuous-wave output power of 0.81 W at 1866-1947 nm with a slope efficiency of 71.2% (versus the absorbed pump power) and showed a laser threshold of 200 mW. The waveguide propagation losses were as low as 0.3±0.2 dB/cm. The laser performance under in-band pumping was superior compared pumping at ~800 nm ($^3H_6 \rightarrow {}^3H_4$ transition), i.e., the conventional pump wavelength. Vibronic laser emission from the WG laser above 2 μm is also achieved. The low-loss behavior, the broadband emission properties and good power scaling capabilities indicate the suitability of Tm^{3+}:CALGO waveguides for mode-locked laser operation at ~2 μm.

1. Introduction

Femtosecond (fs) Direct Laser Writing (DLW), also known as Ultrafast Laser Inscription (ULI) is a powerful method for the fabrication of passive and active photonic micro-structures such as optical waveguides (WGs) in transparent dielectric materials [1-3]. These materials absorb the energy of the fs pulses through nonlinear processes, leading to a permanent modification of the structure at the μm-scale and, consequently, a change of the refractive index Δn with respect to the unmodified (bulk) regions [1]. The advantages of fs-DLW include the fast fabrication time, short interaction time preventing serious damage of the

material, high precision, a wide range of suitable materials (i.e., glasses, ceramics or crystals) and the ability to fabricate 3D structures as building blocks of photonic integrated circuits [4].

The classification of fs-DLW WGs is based on the refractive index change Δn which can be either positive or negative. In type I WGs (for $\Delta n > 0$), the mode guiding is observed *within* the irradiated area (typically, in the form of a damage track). Such conditions are common for amorphous materials such as glasses [5,6] and certain crystals [7]. In type II WGs (for $\Delta n < 0$), the guiding is achieved *between* a pair of damage tracks (the "dual-line" approach) or in the *vicinity* of a single track [8,9]. Within the irradiated areas, the refractive index decreases and between (near) the tracks, it is enhanced due to the photo-elastic effect. Note that the modification of the material associated with the type I WGs is typically not very stable or even can be completely removed under elevated temperatures [1]. In contrast, this is not happening for type II structures which preserve their properties at increased temperature.

Another geometry of depressed-index WGs was proposed [10] and classified as type III structures [1]. In type III WGs, the core is surrounded by a number of closely located damage tracks forming a quasi-continuous "wall" of reduced refractive index. The guided mode is then a bit separated from the WG cladding potentially reducing the propagation losses. Moreover, this approach allows one to control the transverse mode profile [11]. The circular geometry of depressed-index WGs is also attractive because it can be potentially used in combination with the optical fibers.

WG lasers emitting in the eye-safe spectral range near ~2 μm are of interest for optical communications, spectroscopy, sensing of relevant bio- and atmospheric molecules, and for further wavelength conversion to the mid-IR. It is common to achieve ~2 μm laser emission using thulium (Tm^{3+}) or holmium (Ho^{3+}) ions. Tm^{3+} ions typically feature large Stark splitting of the ground-state ($^3H_6$) leading to broadband luminescence and, thus, they are of interest for wavelength-tunable and ultrashort-pulse oscillators.

So far, efficient Tm WG lasers based on Liquid Phase Epitaxy (LPE) technology were demonstrated [12,13]. Van Dalfsen *et al.* reported on a Tm:$KY_xGd_yLu_z(WO_4)_2$ channel WG laser delivering up to 1.6 W at 1.84 μm with a slope efficiency of 75–81% employing a conventional pumping scheme (for the $^3H_6 \rightarrow {}^3H_4$ transition, at ~0.8 μm) [12]. For thulium WG lasers fabricated by fs-DLW, typically, lower output powers were extracted [14-19]. This can be explained by several reasons. First, in many studies, Tm^{3+}-doped glasses were used for fabrication of WGs and the power scaling was limited by poor thermo-mechanical properties of the glass. Second, the WG propagation losses in such structures still have to be reduced (as compared to LPE-based devices). Third, the use of high-brightness pump sources, such as Ti^{3+}:Sapphire lasers, limited the available pump power. Lancaster *et al.* demonstrated a fs-DLW channel WG laser in bulk Tm:ZBLAN glass generating 205 mW at 1.89 μm and reaching a slope efficiency of 67% [15]. Note that for conventional pumping, to reach high slope efficiency, one needs to rely on the cross-relaxation for adjacent Tm^{3+} ions [12] leading to the requirement of high Tm^{3+} doping. High doping may lead to lower quality of the crystal, deformation of its lattice (thus, higher passive losses) or it may raise the efficiency of parasitic spectroscopic processes such as energy-transfer upconversion or energy-migration.

Further advances in the field of fs-DLW Tm WG lasers require (i) the search for novel materials supporting power-scalable laser operation and (ii) the introduction of an alternative pumping scheme, which may intrinsically bring the advantage of high laser efficiency at any Tm^{3+} doping levels. Towards the first goal, in this work, we propose to use Tm^{3+}-doped calcium gadolinium aluminate ($CaGdAlO_4$ abbreviated as CALGO). This host material was first considered for Yb^{3+} doping [20] leading to high-power [21] and ultrashort-pulse mode-locked [22,23] lasers, including thin-disk lasers [24]. The key advantages of rare-earth doped CALGO are (i) good thermal properties, namely high thermal conductivity showing a weak dependence on the doping level [25] with weak and positive thermal lensing [26], and (ii) a structural disorder leading to inhomogeneous broadening of the spectral bands [27]. Channel WG lasers were fabricated in bulk Yb^{3+}:CALGO by fs-DLW [28,29]. Hasse *et al.* reported on

a WG laser based on the dual-line approach (type II) generating 2.4 W of output power at 1030–1042 nm with a slope efficiency of 69% (WG propagation losses of ~1.1 dB/cm) [28].

The CALGO crystal and its yttrium isomorph (CALYO) were also implemented for Tm^{3+} doping. Hutchinson *et al.* first reported on spectroscopy of Tm:CALYO crystals [30]. Laser operation was first achieved by Moncorge *et al.* [31]. Recent studies focused on diode-pumped laser performance and wavelength tuning [32]. Wang *et al.* demonstrated a SESAM mode-locked Tm:CALGO bulk laser generating 650 fs pulses at 2021 nm (emission bandwidth: ~9 nm) at a repetition rate of ~100 MHz [33].

The second goal is reached by implementing the so-called in-band or resonant pumping directly exciting the electrons to the upper laser level ($^3F_4$). This concept has been already demonstrated for bulk Tm lasers. W. Yao *et al.* developed an in-band-pumped Tm^{3+}:CALYO laser delivering 6.8 W at 1968 nm with a slope efficiency of ~56% [34]. Recently, it was implemented for Tm WG lasers based on the LPE fabrication technology: Loiko *et al.* achieved 2.05 W at 1881 nm with a very high slope efficiency of 78.3% [35]. The advantages of in-band pumping are high slope efficiencies approaching the Stokes limit even at low Tm^{3+} doping levels and reduced heat loading.

In the present work, we demonstrate the first Tm^{3+}:CALGO waveguide laser based on the fs-DLW fabrication method and implementing the in-band pumping scheme for reaching high slope efficiency and power scalability approaching the watt-level output.

2. Fabrication and characterization of waveguides

2.1 Femtosecond direct laser writing

As a gain material, we used bulk Tm:CALGO crystals grown by the conventional Czochralski method using Ar atmosphere in an Ir crucible and an [001]-oriented undoped seed [32]. Tm:CALGO is tetragonal (sp. gr. *I*4/*mmm* - D^{17}_{4h}). The crystal composition was determined by Inductively Coupled Plasma Mass Spectrometry (ICP-MS) as $CaGd_{0.913}Lu_{0.052}Tm_{0.035}AlO_4$. The actual concentration of Tm^{3+} ions N_{Tm} was 4.31×10^{20} cm^{-3} (3.5 at.% Tm).

The laser crystal (thickness *t*: 6.2 mm, aperture: 3.2×3.1 mm^2) was cut for light propagation along the crystallographic ***c***-axis (***c***-cut), i.e. for σ-polarization. Both its input and output faces were polished to a laser-grade quality and left uncoated.

Depressed-index WGs were fabricated in bulk Tm:CALGO by fs-DLW. Two types of structures were produced, namely buried channel WGs with a circular cladding (diameter: 60, 80 and 100 μm), and surface channel WGs with a half-ring cladding (diameter: 60 μm). The WG cladding was formed by a set of continuous damage tracks produced in the crystal by fs laser radiation. Light guiding is expected in the core located within the cladding showing a decreased refractive index ($\Delta n = n_{track} - n_{bulk} < 0$), Fig. 1. Note that among the approaches of WG fabrication based on fs-laser irradiation, the surface WGs can be easily fabricated only in the depressed cladding geometry.

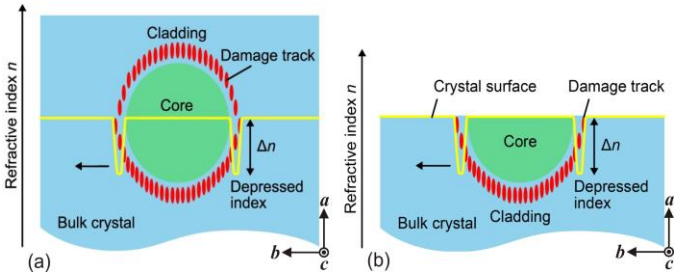

Fig. 1. Geometries of depressed-index (a) buried and (b) surface channel WGs (type III) fabricated in bulk Tm:CALGO crystal by fs-DLW.

For fs-DLW, we employed 120-fs, 795-nm pulses from a Ti:Sapphire regenerative amplifier operating at a repetition rate of 1 kHz [36]. The laser output was focused into the

sample through the polished top surface using a 40× microscope objective (N.A. = 0.65). Only a small fraction of the pulse energy was utilized and controlled with a λ/2 plate, a neutral density filter and a polarizer. The writing parameters were optimized in a set of test experiments as follows: incident pulse energy of 0.25 μJ (buried WGs) and 0.17 μJ (surface one), writing speed of 400 μm/s and track separation of 3 μm. To produce the damage tracks, the crystal was repetitively translated along its ***c***-axis. The tracks were written along the entire length of the crystal. No post-writing repolishing of the crystal surfaces was applied as they were preserved undamaged.

The refractive index contrast Δn for similar depressed-cladding WGs fabricated in another oxide crystal was estimated to be about ~1×10^{-3} [18,19]. The authors of Refs. [28,29] did not specify Δn for WGs fabricated by fs-DLW in Yb^{3+}:CALGO.

2.2 Bulk crystal spectroscopy

Here, we briefly describe the spectroscopic properties relevant for laser operation. In the CALGO crystal, the Ca^{2+} and $Gd^{3+}|Lu^{3+}$ cations are statistically distributed over the same type of sites (C_{4v} symmetry, IX-fold oxygen coordination). The Tm^{3+} ions replace the Gd^{3+} cations. The local disorder originates from the second coordination sphere of Tm^{3+} [27]. Consequently, smooth and broad spectral bands both in absorption and emission are observed. This effect is even further promoted by the introduction of Lu^{3+} cations which replace in part the Gd^{3+} ones [32] (note that the Lu^{3+} ions are optically passive).

CALGO is an optically uniaxial crystal (the optical axis is parallel to the ***c***-axis), so that there are two principal light polarizations, π and σ. At the wavelength of ~1.92 μm, its refractive indices are $n_o = 1.9021$ and $n_e = 1.9249$ [37].

The absorption cross-section spectra, σ_{abs}, for the transition from the $^3H_6$ ground-state to the excited-states of Tm^{3+} in CALGO, $^3H_4$ (conventional pumping) and $^3F_4$ (in-band pumping), are shown in Fig. 2(a) for π and σ polarizations. For the $^3H_6 \rightarrow {}^3H_4$ transition, σ_{abs} is 0.67×10^{-20} cm^2 at 798 nm and the full width at half maximum (FWHM) of the absorption band is 18.6 nm. For the $^3H_6 \rightarrow {}^3F_4$ one, $\sigma_{abs} = 0.65\times10^{-20}$ cm^2 at 1736 nm with a larger FWHM of 120 nm. Here, all values are specified for σ-polarization as all the rays propagating along the ***c***-axis correspond to this polarization state.

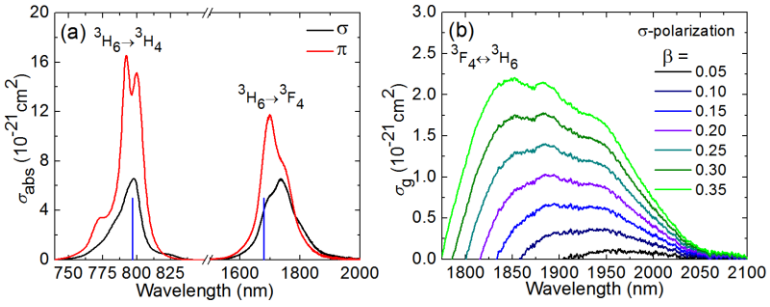

Fig. 2. Spectroscopy of Tm^{3+} ions in tetragonal CALGO crystals: (a) absorption cross-sections, σ_{abs}, for the $^3H_6 \rightarrow {}^3H_4$ and $^3H_6 \rightarrow {}^3F_4$ transitions (π and σ light polarizations), *blue lines* indicate the pump wavelengths in this work. After [32]; (b) gain cross-sections, $\sigma_g = \beta\sigma_{SE} - (1 - \beta)\sigma_{abs}$, for σ-polarization, $\beta = N_2(^3F_4)/N_{Tm}$ is the inversion ratio for the $^3F_4 \rightarrow {}^3H_6$ transition. Calculated from Ref. [32].

For the $^3F_4 \rightarrow {}^3H_6$ laser transition, the maximum stimulated-emission (SE) cross-section σ_{SE} is 0.91×10^{-20} cm^2 at 1813 nm for σ-polarization, calculated by the Füchtbauer–Ladenburg method, see Ref. [32] for the details. Tm lasers operating on this transition represent a quasi-three-level laser scheme exhibiting reabsorption. To quantify this, the gain cross-sections for several inversion ratios are calculated in Fig. 2(b) for σ-polarization. The gain spectra of Tm:CALGO are smooth and broad. For an inversion ratio β of 0.20, the gain bandwidth is ~145 nm. The upper laser level lifetime of Tm:CALGO τ_{Tm} is ~3.2 ms [32].

2.3 Confocal microscopy

The geometry of the fabricated WGs was studied using a confocal laser microscope LSM 710 (Carl Zeiss). It was equipped with a rotatable polarizer (P), analyzer (A) and a blue GaN laser (λ = 405 nm).

At first, we looked at one of the crystal end-facets in polarized light (P || ***a***-axis). The confocal microscope image for the buried WG with a circular cladding is shown in Fig. 3(a). One can clearly see the WG cladding formed by individual damage tracks which appears darker than the surrounding bulk material, due to light scattering. The measured diameter of the cladding is 106 × 104 μm (horizontal × vertical), which is close to the targeted value (~100 μm). The size of each individual damage track is 2 × 6 μm. This asymmetry is determined by the writing geometry (through the top surface). The separation between the tracks is ~3 μm (horizontal) and 0–6 μm (vertical). The axis of the WG is located at ~130 μm below the crystal surface. The area inside the cladding appears slightly darker (the greyscale colors are enhanced) possibly due to partial coupling of light into the WG and scattering at the cladding. There are no cracks originating from the fs-DLW.

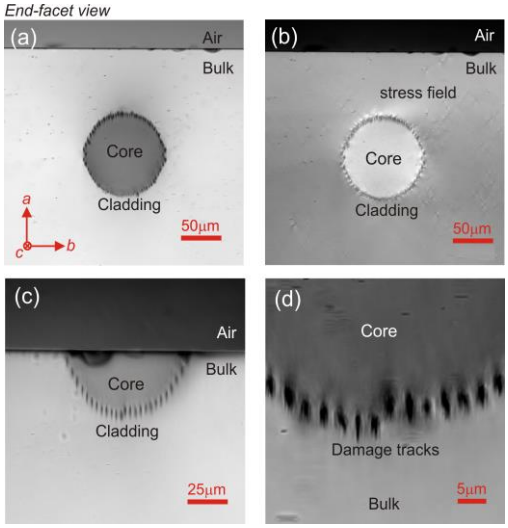

Fig. 3. WG end-face inspection: Confocal laser microscope images of depressed-index fs-DLW WGs in Tm:CALGO crystal: (a,b) buried WG with circular cladding (size: 100 μm); (c,d) surface WG with half-ring cladding (size: 60 μm). End-facet view, transmission mode, λ = 405 nm, light polarization (***E*** || ***a***) is vertical. Image (b) is obtained in crossed polarizers.

By inspecting the same WG placed between two crossed polarizers (P || ***a***, A || ***b***), see Fig. 3(b), we observed a clear enhancement of the light intensity inside the WG cladding and around it. This is ascribed to the stress fields [38] caused by fs-DLW and inducing a local change of the optical indicatrix via the photo-elastic effect.

A similar study is performed for the surface WG, Fig. 3(c). The measured size of this WG is 72 × 40 μm (horizontal × vertical). The WG is located just beneath the crystal surface: the distance to the most shallow damage tracks is only 6 μm. The cracks in Fig. 3(c) originate from polishing of the WG end-facet before the fabrication of the WG. Figure 3(d) gives a close look on individual damage tracks.

Subsequently, we examined the top surface of the sample in polarized light (P || ***c***). The canvas-like barrel-shape cladding of the buried WGs is clearly seen in Fig. 4(a). No cracks are observed in the surrounding bulk region. By observing the individual damage tracks, Fig. 4(b), we conclude that they are continuous along the writing direction. The width of the tracks is ~1 μm and the deviation from a straight line is less than 2 μm.

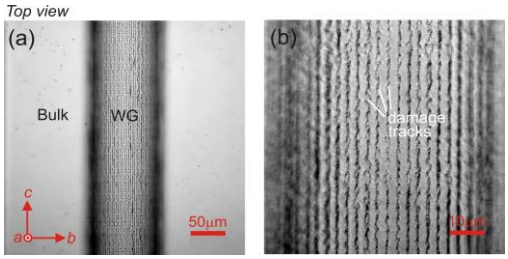

Fig. 4. WG top-surface inspection: Confocal laser microscope images of depressed-index fs-DLW WGs in Tm:CALGO crystal: (a,b) buried WG with a circular cladding (size: 100 μm). Top-view, transmission mode, λ = 405 nm, light polarization (***E*** || ***c***) is vertical.

2.4 μ-Raman spectroscopy

Raman spectroscopy is sensitive to weak modifications of the structure of the host material. For μ-Raman studies, we used a Renishaw inVia Reflex confocal Raman microscope equipped with a 50× Leica objective and an Ar^+ ion laser (λ = 514 nm).

The Raman spectrum of the ***c***-cut Tm:CALGO crystal is shown in Fig. 5. The maximum phonon energy is ~650 cm^{-1}.

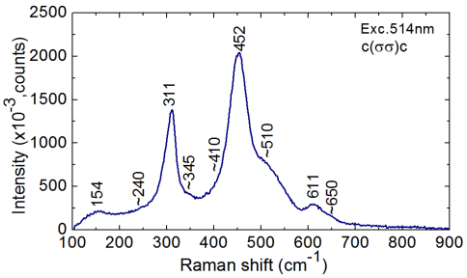

Fig. 5. Raman spectrum of the ***c***-cut Tm:CALGO bulk crystal. The measurement geometry is ***c***(σσ)***c***, λ_{exc} = 514 nm. The *numbers* indicate the Raman frequencies in cm^{-1}.

For μ-Raman mapping of the crystal end-facet, we selected the vibration at ~452 cm^{-1} and monitored this Raman peak intensity, width and position. The results for the buried WG with a circular cladding (diameter: 100 μm) are shown in Fig. 6. In the area containing the damage tracks, the Raman peak intensity decreases, the peak is broadened and a shift of its position is observed. These changes indicate modification of the material in the irradiated area, in particular, a reduction of its crystallinity [39]. In Fig. 6(b),(c), one can also see a slight variation of the Raman response in the areas outside the cladding which are spatially matching the stress fields suggested by the confocal microscopy study, Fig. 3(b). In the WG core, the Raman response of the material is very close to that in the bulk crystal, confirming no alteration of the crystal structure in the core.

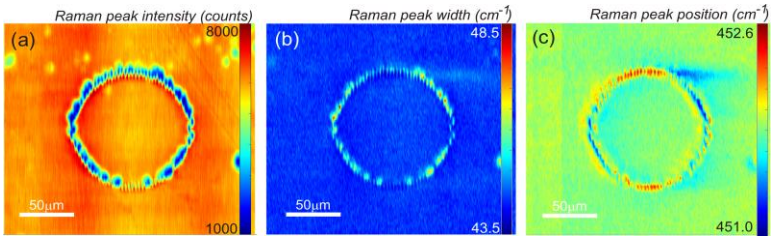

Fig. 6. μ-Raman mapping of a depressed-index buried channel WG with a circular cladding (size: 100 μm) fabricated in a Tm:CALGO crystal by fs-DLW: (a) peak intensity, (b) width (FWHM), (c) position; monitoring the ~452 cm^{-1} mode in the ***c***(σσ)***c*** geometry, λ_{exc} = 514 nm.

3. Laser operation

3.1 Laser set-up

The scheme of the in-band pumped WG laser is shown in Fig. 7(a). The crystal containing the WGs was mounted on a passively-cooled Cu-holder using a silver paste for better heat removal. The laser cavity was formed by a flat pump mirror (PM) coated for high transmission (HT, T = 93.0%) at 1.68 μm and for high reflection (HR) at 1.86-2.32 μm, and a set of flat output couplers (OCs) with transmissions T_{OC} in the range of 1.5%–50% at the laser wavelength. The OCs were transmittive for the pump radiation. We also used a band-pass OC supporting laser oscillation above 2 μm (coating specification: HT at 1.80–1.96 μm, T = 1.5% at 2.03–2.20 μm). Both the PM and the OC were placed as close as possible to the crystal. No index-matching liquid was used to avoid damage to the optical elements.

As a pump source for in-band pumping ($^3H_6 \rightarrow {}^3F_4$ transition), we used a home-made Raman fiber laser (RFL) delivering up to 2.9 W of linearly polarized output at 1679 nm ($M^2 \approx 1$, emission bandwidth: < 1 nm) [40]. The fundamental beam was provided by an erbium fiber master oscillator power amplifier (MOPA) configuration. The RFL was based on a single-mode polarization maintaining germanosilicate fiber (iXBlue Photonics; core diameter, 4.5 μm; length, 300 m) exhibiting a Raman-active mode with energy of ~440 cm^{-1}. The output of the RFL was collimated with a lens (focal length: f = 7.5 mm), filtered from the residual pump at 1560 nm using a beam-splitter and focused into the crystal through the PM with an uncoated spherical CaF_2 lens (f = 40 mm).

The measured pump spot diameter in the focus $2w_P$ was 30±5 μm. The pump coupling efficiency $\eta_{coupl} = P_{coupl}/P_{inc}$ was simply estimated from the Fresnel losses at the uncoated input crystal facet to be 90.3% (n_o = 1.9055 [37]) because we were unable to detune the pump wavelength out of Tm^{3+} absorption for direct measurements. This does not overestimate the laser slope efficiency. Note that the estimated numerical aperture of the depressed-cladding WG is N.A. = 0.06 (calculated using the approximate expression for step index waveguides $N.A.^2 \approx 2n\Delta n$ for n = 1.905 at 1.68 μm (for the *o*-wave) and $\Delta n \approx -1\times10^{-3}$. It exceeds the numerical aperture of the pump beam, N.A. = $n\times\sin[\lambda/(n\pi w_P)]$ = 0.036 (calculated for $w_P \approx 15$ μm and taking into account the beam quality parameter $M^2 \approx 1$, see above). The single-pass pump absorption was calculated from the small-signal value (in the limit of absent ground-state bleaching), $\eta_{abs,0(1\text{-pass})} = 1 - \exp(-\sigma^P_{abs} N_{Tm} t)$ = 64.5% ($\sigma^P_{abs} = 0.40\times10^{-20}$ cm^2 is the absorption cross-section at the pump wavelength λ_P for σ-polarization). In reality, due to the ground-state bleaching, the pump absorption under lasing conditions will be lower. The estimated saturation power, $P_{sat} = [A_P h\nu]/[(\sigma^P_{abs} + \sigma^P_{SE})\tau_{Tm}]$ is about 180 mW for the 60 μm-diameter WG (here, A_P is the pump mode area).

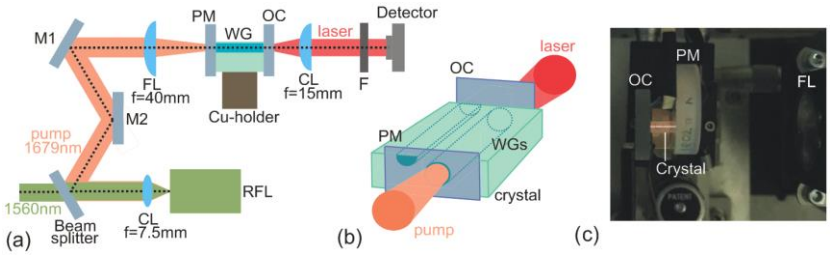

Fig. 7. Scheme of the in-band-pumped Tm:CALGO WG laser: (a) laser set-up, CL and FL – collimating and focusing lens, respectively, M1 and M2 – folding mirrors, PM – pump mirror, OC – output coupler, WG – waveguide, F – dichroic mirror, RFL – Raman fiber laser; (b) geometry of the studied WG lasers (buried and surface); (c) photograph of the laser.

The geometry of the buried and channel WG lasers is shown in Fig. 7(b). A photograph of this laser is presented in Fig. 7(c). The weak visible (white) emission from the WG is related to upconversion luminescence of laser-active Tm^{3+} ions and impurity Er^{3+} ones.

The laser emission after the OC was collimated using a spherical CaF_2 lens (f = 15 mm) and filtered from the residual pump using a dichroic mirror. The spectra of laser emission were measured using an optical spectrum analyzer (model AQ6375B, Yokogawa). The beam profile was captured using a FIND-R-SCOPE near-IR camera.

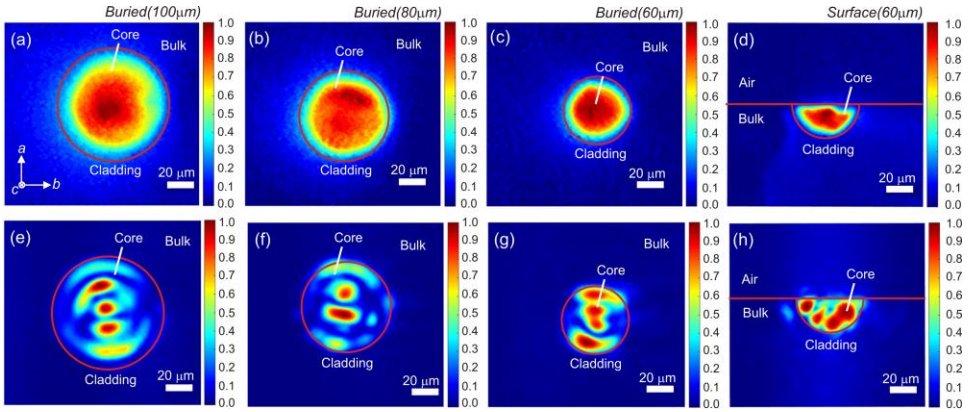

Fig. 8. Near-field pump modes for depressed-index fs-DLW channel WGs in Tm:CALGO: top row: (a)-(c) λ_P = 798 nm, bottom row: (e)-(f) λ_P = 1679 nm; buried WGs with a circular cladding and a diameter of (a,e) 100 μm, (b,f) 80 μm, (c,g) 60 μm and (d,h) surface WG with a half-ring cladding (size: 60 μm). The *red circular lines* indicate the cladding / crystal surface and are drawn as a guide for the reader.

A similar set-up was used for pumping at ~800 nm ($^3H_6 \rightarrow {}^3H_4$ transition), e.g., the conventional pump wavelength. For this, we employed a Ti:Sapphire laser (model Mira 900, Coherent) emitting up to 1.5 W at λ_P = 798 nm ($M^2 \approx 1$). The pump light was collimated using a microscope objective (Mitutoyo M Plan NIR 10×, N.A. = 0.28, f = 20 mm, T = 63.8% at 0.80 μm) resulting in $2w_P = 20\pm5$ μm. The flat PM was coated for HT ($T > 99\%$) at 0.80 μm and for HR at 1.8–2.1 μm and the set of flat OCs had a transmission T_{OC} of 1.5%–30% at the laser wavelength. The residual pump was filtered with a long-pass filter (FEL1000, Thorlabs).

The pump coupling efficiency was estimated from the pump-transmission measurements at ~850 nm (outside the Tm^{3+} absorption), e.g., for the buried WG with a circular cladding (size: 60 μm), η_{coupl} = 81±2% (including the Fresnel losses, subtracting the WG propagation losses of 0.6 dB/cm, see below). Similarly to the analysis performed for in-band pumping, we estimated the numerical aperture of the depressed-cladding WG, N.A. = 0.06, which exceeds that of the pump beam, N.A. = 0.027 (as calculated for $w_P \approx 10$ μm and the beam quality parameter $M^2 \approx 1$). The pump absorption at the threshold pump power was determined from similar measurements at 798 nm, $\eta_{abs,L(1\text{-}pass)}$ = 83±2%, being close to the small-signal one.

The near-field profiles of the pump modes for the conventional (λ_P = 798 nm) and in-band (λ_P = 1679 nm) pumping are shown in Fig. 8. For λ_P = 798 nm, the pump radiation almost uniformly fills the volume of the WG core. In this case, a short-pass filter was used to filter out the ~2 μm fluorescence signal from Tm^{3+}. At the wavelength of λ_P = 1679 nm, less modes are supported. This is attributed in part to the difference in the pump wavelengths and to the fact that larger pump beam excites less transverse modes in the WG. Still, the modes are well confined within the WG cladding (its position is marked by red circles). In the latter case, part of the detected signal can be related to the fluorescence of Tm^{3+} ions.

3.2 WG laser pumped at 798 nm - conventional pumping

We started the laser experiments using the conventional pumping (λ_P = 798 nm). The input-output dependences for the buried channel WG (diameter: 60 μm) are presented in Fig. 9(a). The WG laser generated a maximum output power of 0.27 W at 1824-1832 nm with a slope efficiency η of 50.3% (vs. the calculated absorbed pump power P_{abs}) and a laser threshold of

P_{th} = 92 mW. The optical-to-optical efficiency η_{opt} was 29.6% (vs. the incident power on the crystal). The highest output power corresponded to T_{OC} = 30% (the maximum available output coupling in this experiment). With increasing the output coupling from 1.5% to 30%, the laser threshold gradually increased from 40 mW to 92 mW. We did not observe any thermal roll-over in the output dependences, damage of the WG end-facets or fracture of the WG itself. For lower output coupling, the slope efficiency gradually decreased.

The determined value of the slope efficiency for T_{OC} = 30% exceeds the limit set by the Stokes efficiency, $\eta_{St} = \lambda_P/\lambda_L$ = 43.6% ($\lambda_L \approx$ 1830 nm is the laser wavelength), which indicates the effect of cross-relaxation between adjacent Tm^{3+} ions.

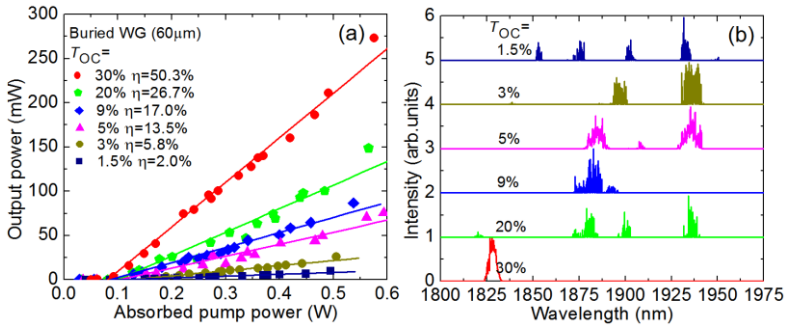

Fig. 9. Fs-DLW Tm:CALGO channel waveguide laser pumped at λ_P = 798 nm (conventional pumping): (a) input-output dependences, η – slope efficiency; (b) laser emission spectra measured at P_{abs} = 0.4 W. Buried WG with a circular cladding (diameter: 60 μm).

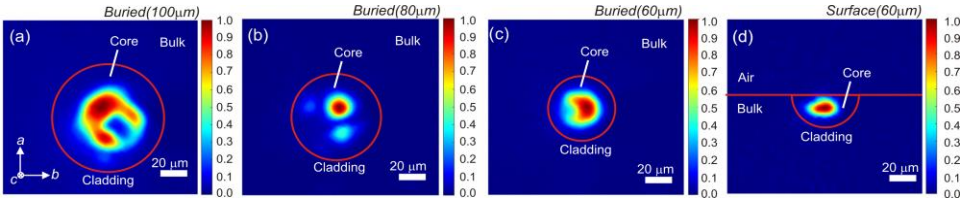

Fig. 10. Near-field spatial profiles of the laser mode for Tm:CALGO WG lasers using conventional pumping (λ_P = 798 nm): (a)-(c) buried WGs with a circular cladding (diameter: (a) 100 μm, (b) 80 μm, (c) 60 μm); (d) surface WG with a half-ring cladding (size: 60 μm). The *red circular lines* indicate the cladding / crystal surface and are drawn as a guide for the reader. T_{OC} = 20%.

Typical laser emission spectra are shown in Fig. 9(b). For T_{OC} < 30%, the emission occurred in several spectral regions, at 1.85, 1.88, 1.90 and 1.93 μm. For example, for the lowest studied T_{OC} = 1.5%, it was at 1851–1936 nm. This spectral behavior is attributed to the broad gain spectra of Tm:CALGO, Fig. 2(b). Let us analyze this in more details. According to the gain spectra, an inversion level of $\beta \approx$ 10% is needed to explain the observed multi-line spectral behavior for this OC. The peak gain cross-section is then $\sigma_g = 0.36\times10^{-21}$ cm^2 at 1.94 μm. Indeed, the maximum in the laser emission spectrum is observed at 1932 nm. Thus, the round-trip gain, $G = \exp(\sigma_g N_{Tm} 2t)$, amounts to 0.84 dB. Accounting for the output-coupling losses, we achieve an estimation for the WG propagation losses: δ_{loss} = 0.62 dB/cm. For T_{OC} = 30%, the emission wavelength was shorter, at 1.83 μm. This difference was in part originating from the mirrors which provided flat reflectivity in the range of 1.84–2.1 μm. The laser emission was unpolarized in all cases.

Typical modes of laser emission in the near-field for all four studied WGs are shown in Fig. 10. The laser modes are clearly different from the pump ones, Fig. 8(a)-(d). This is because less transverse modes are supported for the same Δn at longer wavelengths and because of mode competition. In all cases, the laser mode was well confined within the WG cladding following the pumped area.

3.3 WG laser pumped at 1679nm - in-band pumping

The performance of the buried channel WG laser (size: 60 μm) for different output coupling is shown in Fig. 11(a). The WG laser generated a maximum output power of 0.81 W at 1866-1947 nm with a slope efficiency η of 71.2% and showed a laser threshold P_{th} of 200 mW. The optical-to-optical laser efficiency η_{opt} amounted to 35.8%. These results were achieved for the optimum T_{OC} of 30%. For higher output coupling (T_{OC} = 50%), the efficiency deteriorated (η = 47.2%) and the laser threshold increased (to P_{th} = 275 mW) probably due to the enhanced upconversion related to high population inversion. Despite the energy-transfer upconversion mostly affects the laser threshold, it may affect the slope efficiency in an indirect way (e.g., via the related heat loading). The unpolarized laser emission was broadband, Fig. 11(b), similar as in the case of pumping at 798 nm, Fig. 9(b), due to the flat and broad gain spectra. Let us apply the gain calculation (Section 3.2) in this case. For the smallest T_{OC} = 1.5%, the observed peak laser wavelength corresponds to an inversion ratio $\beta \approx 6\%$, so that the peak $\sigma_g = 0.16\times10^{-21}$ cm^2 at 1.96 μm. This gives the value of the round-trip gain G = 0.37 dB and the estimation for the WG propagation losses δ_{loss} = 0.25 dB/cm. The spectral behavior was also determined by the etalon (Fabry-Perot) effects at the crystal / mirror interfaces. The air gaps at the PM / crystal and the crystal / OC interfaces were about 200–400 μm.

The maximum slope efficiency achieved for in-band pumping (71.2%) is higher than that for the conventional pumping scheme (50.3%). Considering the same range of absorbed pump powers ($P_{abs} \le 0.6$ W), both pump schemes lead to a similar level of the output power. As the RFL provided higher available power level, the power scalability of the in-band pumped WG laser was much better.

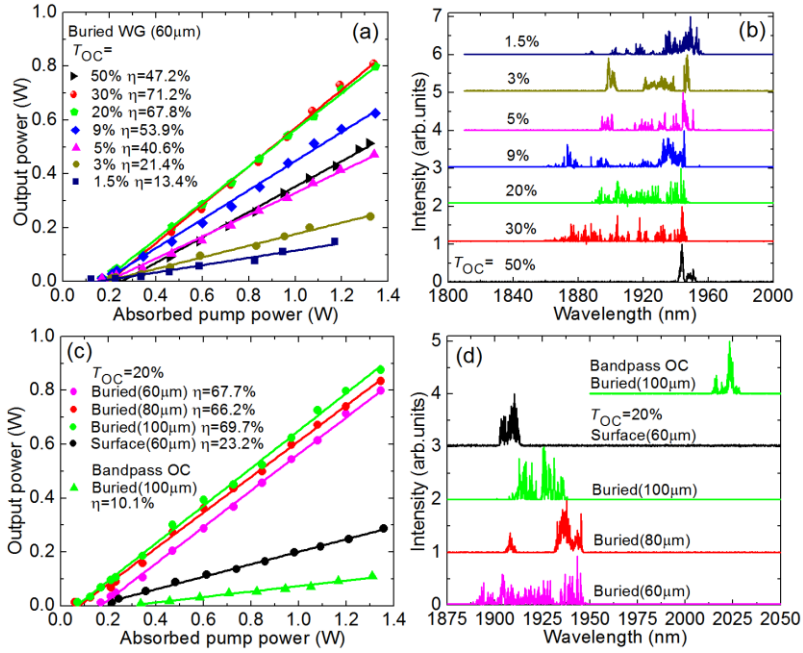

Fig. 11. Fs-DLW Tm:CALGO channel waveguide lasers in-band pumped at 1679 nm: (a,b) buried WG with a circular cladding (size: 60 μm), (c,d) comparison of buried (size: 60–100 μm) and surface (size: 60 μm) WGs, T_{OC} = 20%, (a,c) input-output dependences, η – slope efficiency; (b,d) typical laser emission spectra measured at P_{abs} = 1.5 W.

The comparison of the laser performance of all four studied WGs is shown in Fig. 11(c) for the same T_{OC} = 20%. For the buried WGs, the output power increased slightly with the WG diameter and the threshold decreased, reaching 0.88 W at 1907–1938 nm with η = 69.7% and P_{th} = 70 mW for the WG with the largest cross-section (100 μm). Thus, the propagation

losses increase for WGs with a smaller diameter. The performance of the surface WG was inferior which is attributed to higher propagation losses: the surface WG laser generated 0.29 W at 1902–1913 nm with lower η of 23.2% and increased P_{th} of 210 mW. The laser emission spectra of different WG lasers are shown in Fig. 11(d) and they are similar.

The WG propagation losses were estimated from the Caird analysis [41], $\delta_{loss} \approx 0.3 \pm 0.2$ dB/cm (for the buried channel WG with a diameter of 60 μm and λ_P = 1679 nm), Fig. 12. A similar calculation based on the laser performance under conventional pumping (λ_P = 798 nm) yields $\delta_{loss} \approx 0.6 \pm 0.3$ dB/cm. Higher propagation losses in the latter case are attributed to (i) stronger overlap of the pump and laser modes with the WG cladding and (ii) higher fractional heat loading under conventional pumping leading to stronger heat dissipation in the WG. The δ_{loss} value for the in-band pumping is comparable to that estimated for fs-DLW depressed-index WGs in bulk Tm^{3+}:ZBLAN glass (0.4±0.2 dB/cm) [15]. As compared to the previously reported type II WGs in Yb^{3+}:CALGO [28], we measured much lower propagation losses.

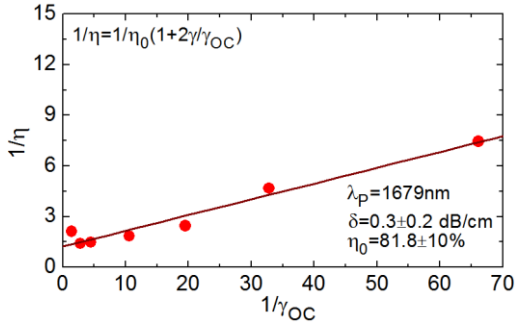

Fig. 12. Caird analysis of intracavity losses in the in-band pumped Tm:CALGO buried WG laser (circular cladding with a diameter of 60 μm): inverse of the slope efficiency, $1/\eta$, vs. inverse of the output-coupling loss, $1/\gamma_{OC}$, *circles* – experimental data, *line* - their fit.

By implementing the band-pass OC, we achieved laser emission above 2 μm: the buried channel WG laser (diameter: 100 μm) generated up to 0.11 W at 2015–2028 nm. However, lasing at such long wavelengths was at the expense of a reduced slope efficiency (η = 10.1%) and an increased laser threshold (P_{th} = 335 mW). Let us analyze this operation regime. The Stark splitting for Tm^{3+} ions in CALGO is unknown. For the isostructural Tm:CALYO crystal [30], the longest wavelength of a purely electronic transition $^3F_4 \rightarrow {}^3H_6$ is 1959 nm as it occurs between the sub-levels with energies of 5689 and 584 cm^{-1}. The emission at longer wavelengths can be however observed due to the electron-phonon coupling (vibronic emission) [42]. In particular, the broad low-energy phonon mode at ~154 cm^{-1}, cf. Fig. 4, may participate in this process.

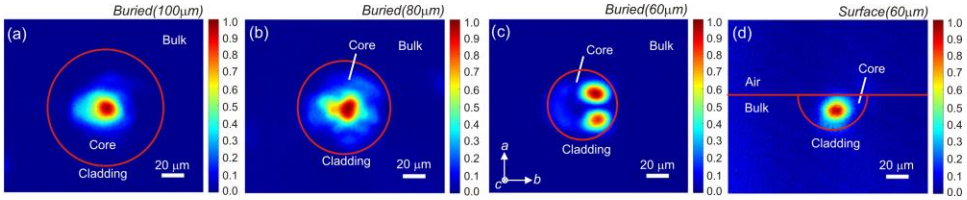

Fig. 13. Near-field profiles of the laser mode for in-band pumped Tm:CALGO WG lasers: (a)-(c) buried WGs with a circular cladding (diameter: (a) 100 μm, (b) 80 μm, (c) 60 μm); (d) surface WG with a half-ring cladding (size: 60 μm). The *red circular lines* indicate the cladding / crystal surface and are drawn as a guide for the reader. T_{OC} = 20%.

Typical laser emission modes for the in-band pumped WG lasers are shown in Fig. 13. The laser modes were well confined within the WG cladding. For all buried WGs, the emission was spatially multimode. For the surface WG, the mode was close to the fundamental transverse one maybe due to the smaller WG volume and stronger mode

competition under higher losses. The difference in the laser modes for conventional and in-band pumping, see Fig. 10 and Fig. 13, is mostly determined by different spatial distribution of the pump inside the WGs.

For in-band pumping, the upper limit for the laser slope efficiency can be estimated from the Stokes one, $\eta_{St} \approx 87\%$. The achieved slope efficiency, Fig. 11(a), is close to this value. The main physical reasons for the reduced η are (i) non-perfect overlap of the pump and laser modes (a single transverse mode WG with a smaller diameter of the cladding is required to optimize the mode overlap) and (ii) possible thermo-optic effects originating from increased heat loading associated with the upconversion losses in Tm^{3+}:CALGO at high inversion ratios β which are expected to be suppressed with the optimization of the Tm^{3+} doping level.

4. Conclusion

The first ~2 μm waveguide lasers based on the CALGO crystalline host have been demonstrated. We have confirmed, Tm^{3+}:CALGO is a suitable crystalline material for efficient and power-scalable 2-μm waveguide lasers due to its high thermal conductivity, good thermo-mechanical properties, and broad and smooth Tm^{3+} emission bands originating from the structural disorder. Employing fs direct laser writing, we have fabricated low-loss depressed-index buried and surface channel waveguides with a circular and half-ring cladding (classified as type III). Confocal laser microscopy and μ-Raman spectroscopy confirmed the well-preserved single-crystalline nature of the material in the WG core region, its modification in the cladding and suggested the role of the stress fields in additional variation of the refractive index. The Tm:CALGO waveguide lasers feature high CW output power (approaching the watt-level), high laser slope efficiency of more than 70% and extremely broadband emission properties (free-running emission: 1866-1947 nm, vibronic emission: 2015–2028 nm). The excellent output performance was achieved employing the in-band pumping scheme.

The proposed scheme of in-band pumping using Raman fiber lasers paves the way towards multi-watt output from fs direct laser written Tm waveguide lasers. Indeed, in the present paper, we were mostly limited by the available power from the RFL. The performance of the RFL can be improved both in terms of the emission wavelength and the output power. The laser wavelength can be shifted up to 1700 nm thus better matching the $^3H_6 \rightarrow {}^3F_4$ Tm^{3+} absorption in CALGO for π-polarization, by pumping the Raman fiber near 1580 nm (erbium L-band). The output power can be scaled to the 10 W level, e.g., by using the random lasing configuration at the expense of broader laser linewidth. We expect that the optimization of the Tm^{3+} doping level and the WG length will allow for a simultaneous control of upconversion losses and pump absorption. Regarding the material, it is also promising to study ***a***-cut crystals giving access to π-polarization showing higher absorption cross-sections and linearly polarized laser output. In the present work, we selected ***c***-cut crystals because of the crystal growth direction.

To the best of our knowledge, there are only Q-switched mode-locking results achieved with Tm^{3+}-doped material based WGs emitting around the 2 μm wavelength range [43]. One of the essential limitations for the lack of CW mode-locking results was because of the rather low intracavity power achievable with the conventional pump scheme. Fs direct laser written Tm^{3+}:CALGO waveguides with a smaller cladding diameters (about 30 μm, as demonstrated in experiments with other oxide crystals) are expected to support a single transverse mode which, together with low propagation losses, broadband emission and the in-band pumping scheme, makes them promising for compact mode-locked oscillators operating at high (GHz-range) repetition rates.

Funding

Spanish Government, MINECO (MAT2016-75716-C2-1-R (AEI/FEDER,UE), FIS2017-87970-R); Junta de Castilla y León (SA287P18); Generalitat de Catalunya (2017SGR755);

French Agence Nationale de la Recherche (LabEx EMC3 project FAST-MIR); European Community (FEDER).

Acknowledgments

E. K. acknowledges financial support from the Generalitat de Catalunya under grants 2016FI_B00844, 2017FI_B100158, and 2018FI_B200123. This work was supported by the Normandie region.

Disclosures

The authors declare no conflicts of interest.

References

1. F. Chen and J. R. Vázquez de Aldana, “Optical waveguides in crystalline dielectric materials produced by femtosecond-laser micromachining,” Laser Photon. Rev. **8**(2), 251-275 (2014).
2. R. R. Gattass and E. Mazur, “Femtosecond laser micromachining in transparent materials,” Nature Photon. **2**(4), 219 (2008).
3. S. Nolte, M. Will, J. Burghoff, and A. Tuennermann, “Femtosecond waveguide writing: a new avenue to three-dimensional integrated optics,” Appl. Phys. A **77**(1), 109-111 (2003).
4. G. D. Marshall, A. Politi, J. C. F. Matthews, P. Dekker, M. Ams, M. J. Withford, and J. L. O’Brien, "Laser written waveguide photonic quantum circuits," Opt. Express **17**(15), 12546-12554 (2009).
5. K. M. Davis, K. Miura, N. Sugimoto, and K. Hirao, “Writing waveguides in glass with a femtosecond laser,” Opt. Lett. **21**(21), 1729–1731 (1996).
6. A. M. Streltsov and N. F. Borrelli, "Study of femtosecond-laser-written waveguides in glasses," J. Opt. Soc. Am. B **19**(10), 2496-2504 (2002).
7. A. Rodenas and A. K. Kar, "High-contrast step-index waveguides in borate nonlinear laser crystals by 3D laser writing," Opt. Express **19**(18), 17820-17833 (2011).
8. J. Siebenmorgen, T. Calmano, K. Petermann, and G. Huber, "Highly efficient Yb:YAG channel waveguide laser written with a femtosecond-laser," Opt. Express **18**(15), 16035-16041 (2010).
9. G. A. Torchia, A. Rodenas, A. Benayas, E. Cantelar, L. Roso, and D. Jaque, “Highly efficient laser action in femtosecond-written Nd:yttrium aluminum garnet ceramic waveguides,” Appl. Phys. Lett. **92**(11), 111103-1-3 (2008).
10. A. G. Okhrimchuk, A. V. Shestakov, I. Khrushchev, and J. Mitchell, "Depressed cladding, buried waveguide laser formed in a YAG:Nd^{3+} crystal by femtosecond laser writing," Opt. Lett. **30**(17), 2248-2250 (2005).
11. H. Liu, Y. Jia, J. R. V. de Aldana, D. Jaque, and F. Chen, "Femtosecond laser inscribed cladding waveguides in Nd:YAG ceramics: Fabrication, fluorescence imaging and laser performance," Opt. Express **20**(17), 18620-18629 (2012).
12. K. van Dalfsen, S. Aravazhi, C. Grivas, S. M. García-Blanco, and M. Pollnau, "Thulium channel waveguide laser with 1.6 W of output power and ~80% slope efficiency," Opt. Lett. **39**(15), 4380-4383 (2014).
13. P. Loiko, R. Soulard, G. Brasse, J.-L. Doualan, B. Guichardaz, A. Braud, A. Tyazhev, A. Hideur, and P. Camy, "Watt-level Tm:$LiYF_4$ channel waveguide laser produced by diamond saw dicing," Opt. Express **26**(19), 24653-24662 (2018).
14. D. G. Lancaster, S. Gross, H. Ebendorff-Heidepriem, K. Kuan, T. M. Monro, M. Ams, A. Fuerbach, and M. J. Withford, "Fifty percent internal slope efficiency femtosecond direct-written Tm^{3+}:ZBLAN waveguide laser," Opt. Lett. **36**(9), 1587-1589 (2011).
15. D. G. Lancaster, S. Gross, A. Fuerbach, H. E. Heidepriem, T. M. Monro, and M. J. Withford, “Versatile large-mode-area femtosecond laser-written Tm:ZBLAN glass chip lasers,” Opt. Express **20**(25), 27503–27509 (2012).
16. Y. Ren, G. Brown, A. Ródenas, S. Beecher, F. Chen, and A. K. Kar, “Mid-infrared waveguide lasers in rare-earth-doped YAG,” Opt. Lett. **37**(16), 3339–3341 (2012).
17. J. Morris, N. K. Stevenson, H. T. Bookey, A. K. Kar, C. T. A. Brown, J.-M. Hopkins, M. D. Dawson, and A. A. Lagatsky, “1.9 μm waveguide laser fabricated by ultrafast laser inscription in Tm:Lu_2O_3 ceramic,” Opt. Express **25**(13), 14910–14917 (2017).
18. E. Kifle, P. Loiko, J. R. V. de Aldana, C. Romero, A. Ródenas, S. Y. Choi, J. E. Bae, F. Rotermund, V. Zakharov, A. Veniaminov, M. Aguiló, F. Díaz, U. Griebner, V. Petrov, and X. Mateos, "Passively Q-switched femtosecond-laser-written thulium waveguide laser based on evanescent field interaction with carbon nanotubes," Photon. Res. **6**(10), 971-980 (2018).
19. E. Kifle, P. Loiko, X. Mateos, J. R. V. de Aldana, A. Ródenas, U. Griebner, V. Petrov, M. Aguiló, and F. Díaz, “Femtosecond-laser-written hexagonal cladding waveguide in Tm:$KLu(WO_4)_2$: μ-Raman study and laser operation,” Opt. Mater. Express **7**(12), 4258-4268 (2017).
20. J. Petit, P. Goldner, and B. Viana, "Laser emission with low quantum defect in Yb:$CaGdAlO_4$," Opt. Lett. **30**(11), 1345-1347 (2005).

21. P. Loiko, J. M. Serres, X. Mateos, X. Xu, J. Xu, V. Jambunathan, P. Navratil, A. Lucianetti, T. Mocek, X. Zhang, U. Griebner, V. Petrov, M. Aguiló, F. Díaz, and A. Major, "Microchip Yb:$CaLnAlO_4$ lasers with up to 91% slope efficiency," Opt. Lett. **42**(13), 2431-2434 (2017).
22. Y. Zaouter, J. Didierjean, F. Balembois, G. Lucas Leclin, F. Druon, P. Georges, J. Petit, P. Goldner, and B. Viana, "47-fs diode-pumped Yb^{3+}:$CaGdAlO_4$ laser," Opt. Lett. **31**(1), 119–121 (2006).
23. P. Sévillano, P. Georges, F. Druon, D. Descamps, and E. Cormier, "32-fs Kerr-lens mode-locked Yb:$CaGdAlO_4$ oscillator optically pumped by a bright fiber laser," Opt. Lett. **39**(20), 6001-6004 (2014).
24. N. Modsching, C. Paradis, F. Labaye, M. Gaponenko, I. J. Graumann, A. Diebold, F. Emaury, V. J. Wittwer, and T. Südmeyer, "Kerr lens mode-locked Yb:CALGO thin-disk laser," Opt. Lett. **43**(4), 879-882 (2018).
25. P. Loiko, F. Druon, P. Georges, B. Viana, and K. Yumashev, "Thermo-optic characterization of Yb:$CaGdAlO_4$ laser crystal," Opt. Mater. Express **4**(11), 2241-2249 (2014).
26. F. Druon, M. Olivier, A. Jaffrès, P. Loiseau, N. Aubry, J. DidierJean, F. Balembois, B. Viana, and P. Georges, "Magic mode switching in Yb:$CaGdAlO_4$ laser under high pump power," Opt. Lett. **38**(20), 4138-4141 (2013).
27. P. O. Petit, J. Petit, Ph. Goldner, and B. Viana, "Inhomogeneous broadening of optical transitions in Yb:$CaYAlO_4$," Opt. Mater. **30**(7), 1093-1097 (2008).
28. K. Hasse, T. Calmano, B. Deppe, C. Liebald, and C. Kränkel, "Efficient Yb^{3+}:$CaGdAlO_4$ bulk and femtosecond-laser-written waveguide lasers," Opt. Lett. **40**(15), 3552-3555 (2015).
29. K. Hasse and C. Kränkel, "Yb:CALGO waveguide laser written with 1 MHz-repetition rate fs-laser," in *Laser Congress 2019 (ASSL, LAC, LS&C)*, OSA Technical Digest (Optical Society of America, 2019), P. ATu1A.7.
30. J. A. Hutchinson, H. R. Verdun, B. H. Chai, B. Zandi, and L. D. Merkle, "Spectroscopic evaluation of $CaYAlO_4$ doped with trivalent Er, Tm, Yb and Ho for eyesafe laser applications," Opt. Mater. **3**(4), 287-306 (1994).
31. R. Moncorgé, N. Garnier, P. Kerbrat, C. Wyon, and C. Borel, "Spectroscopic investigation and two-micron laser performance of Tm^{3+}:$CaYAlO_4$ single crystals," Opt. Commun. **41**(1-2), 29-34 (1997).
32. Z. Pan, P. Loiko, J. M. Serres, E. Kifle, H. Yuan, X. Dai, H. Cai, Y. Wang, Y. Zhao, M. Aguiló, F. Díaz, U. Griebner, V. Petrov, and X. Mateos, ""Mixed" Tm:$Ca(Gd,Lu)AlO_4$ - a novel crystal for tunable and mode-locked 2 μm lasers," Opt. Express **27**(7), 9987-9995 (2019).
33. Y. Wang, G. Xie, X. Xu, J. Di, Z. Qin, S. Suomalainen, M. Guina, A. Härkönen, A. Agnesi, U. Griebner, X. Mateos, P. Loiko, and V. Petrov, "SESAM mode-locked Tm:CALGO laser at 2 μm," Opt. Mater. Express **6**(1), 131-136 (2016).
34. W. Yao, F. Wu, Y. Zhao, H. Chen, X. Xu, and D. Shen, "Highly efficient Tm:$CaYAlO_4$ laser in-band pumped by a Raman fiber laser at 1.7 μm," Appl. Opt. **55**(14), 3730-3733 (2016).
35. P. Loiko, R. Thouroude, R. Soulard, L. Guillemot, G. Brasse, B. Guichardaz, A. Braud, A. Hideur, M. Laroche, H. Gilles, and P. Camy, "In-band pumping of Tm:$LiYF_4$ channel waveguide: a power scaling strategy for ~2 μm waveguide lasers," Opt. Lett. **44**(12), 3010-3013 (2019).
36. E. Kifle, X. Mateos, J. R. V. de Aldana, A. Ródenas, P. Loiko, S. Y. Choi, F. Rotermund, U. Griebner, V. Petrov, M. Aguiló, and F. Díaz, "Femtosecond-laser-written Tm:$KLu(WO_4)_2$ waveguide lasers," Opt. Lett. **42**(6), 1169-1172 (2017).
37. P. Loiko, P. Becker, L. Bohatý, C. Liebald, M. Peltz, S. Vernay, D. Rytz, J. M. Serres, X. Mateos, Y. Wang, X. Xu, J. Xu, A. Major, A. Baranov, U. Griebner, and V. Petrov, "Sellmeier equations, group velocity dispersion, and thermo-optic dispersion formulas for $CaLnAlO_4$ (Ln = Y, Gd) laser host crystals," Opt. Lett. **42**(12), 2275-2278 (2017).
38. H.-D. Nguyen, A. Ródenas, J. R. Vázquez de Aldana, J. Martínez, F. Chen, M. Aguiló, M. C. Pujol, and F. Díaz, "Heuristic modelling of laser written mid-infrared $LiNbO_3$ stressed-cladding waveguides," Opt. Express **24**(7), 7777–7791 (2016).
39. E. Kifle, P. Loiko, C. Romero, J. R. V. de Aldana, A. Ródenas, V. Zakharov, A. Veniaminov, M. Aguiló, F. Díaz, U. Griebner, V. Petrov, and X. Mateos, "Femtosecond-laser-written Ho:$KGd(WO_4)_2$ waveguide laser at 2.1 μm," Opt. Lett. **44**(7), 1738-1741 (2019).
40. R. Thouroude, H. Gilles, B. Cadier, T. Robin, A. Hideur, A. Tyazhev, R. Soulard, P. Camy, J. L. Doualan, and M. Laroche, "Linearly-polarized high-power Raman fiber lasers near 1670 nm," Laser Phys. Lett. **16**(2), 025102-1-5 (2019).
41. J. A. Caird, S. A. Payne, P. R. Staber, A. J. Ramponi, L. L. Chase, and W. F. Krupke, "Quantum electronic properties of the $Na_3Ga_2Li_3F_{12}$:Cr^{3+} laser," IEEE J. Quantum Electron. **24**(6), 1077–1099 (1988).
42. P. Loiko, X. Mateos, S. Y. Choi, F. Rotermund, J. M. Serres, M. Aguiló, F. Díaz, K. Yumashev, U. Griebner, and V. Petrov, "Vibronic thulium laser at 2131 nm Q-switched by single-walled carbon nanotubes," J. Opt. Soc. Am. B. **33**(11), D19-D27 (2016).
43. Y. Jia and F. Chen, "Compact solid-state waveguide lasers operating in the pulsed regime: a review [Invited]," Chin. Opt. Lett. **17**(1), 012302-1-23 (2019).